

# Chiral Metafilms and Surface Enhanced Raman Scattering for Enantiomeric Discrimination of Helicoid Nanoparticles

Martin Kartau, Anastasia Skvortsova, Victor Tabouillot, Shailendra K Chaubey, Polina Bainova, Rahul Kumar, Vasili Burtsev, Vaclav Svorcik, Nikolaj Gadegaard, Sang Won Im, Marie Urbanova, Oleksiy Lyutakov, Malcolm Kadodwala,\* and Affar S. Karimullah\*

Chiral nanophotonic platforms provide a means of creating near fields with both enhanced asymmetric properties and intensities. They can be exploited for optical measurements that allow enantiomeric discrimination at detection levels > 6 orders of magnitude than is achieved with conventional chirally sensitive spectroscopic methods based on circularly polarized light. Here it is shown that surface enhanced Raman spectroscopy (SERS) is such a local probe of the near field environment. It is used to achieve enantiomeric discrimination of chiral helicoid nanoparticles deposited on left- and right-handed enantiomorphs of a chiral metafilm using an achiral molecule as a probe. “Hotter” electromagnetic (EM) hotspots are created for matched combinations of helicoid and metafilms (left-left and right-right), while mismatched combinations leads to significantly “cooler” electromagnetic hotspots. This large enantiomeric dependency on hotspot intensity is readily detected using SERS with the aid of an achiral Raman reporter molecule. In effect SERS is used to distinguish between the different EM environments of the plasmonic diastereomers produced by mixing chiral nanoparticles and metafilms. The work demonstrates that by combining chiral nanophotonic platforms with established SERS strategies new avenues in ultrasensitive chiral detection can be opened.

pharmaceutical to quantum computing. Chirally sensitive, chiroptical spectroscopic methods based on the differential interaction of circular polarized light, such as electronic circular dichroism (CD), are important tools since they provide rapid postsynthesis characterization of materials.<sup>[1]</sup> However, the inherent weakness of CD results in it being far less sensitive than nonchirally sensitive measurements.<sup>[2]</sup> Nanophotonic platforms such as plasmonic/dielectric metamaterials provide strong light-matter interactions that have successfully been utilized to increase the sensitivity in biosensing, chiral detection of (sub) monolayer quantities of the materials ( $\leq$ femtomole), and surface enhanced Raman optical activity (SEROA).<sup>[3–15]</sup> There are two different philosophies for exploiting nanophotonic platforms which will for brevity be termed the “direct” and “indirect” strategies. The direct strategy can be considered an extension of conventional CD methods, in which nanophotonic platforms are used to amplify both the intensities and


chiral asymmetries of electromagnetic (EM) fields, to enhance dichroic responses.<sup>[10,16]</sup> This is an elegant and simple concept; however, it does have weaknesses which may limit potential applications, namely, the near UV region <230 nm that is

## 1. Introduction

Chiral organic and inorganic materials have broad impact in science and technology spanning research areas as diverse as

M. Kartau, V. Tabouillot, S. K. Chaubey, R. Kumar, M. Kadodwala, A. S. Karimullah  
School of Chemistry  
Joseph Black Building  
University of Glasgow  
Glasgow G12 8QQ, UK  
E-mail: malcolm.kadodwala@glasgow.ac.uk;  
affar.karimullah@glasgow.ac.uk

A. Skvortsova, P. Bainova, V. Burtsev, V. Svorcik, O. Lyutakov  
Department of Solid State Engineering  
University of Chemistry and Technology  
Prague 16628, Czech Republic  
N. Gadegaard  
School of Engineering  
Rankine Building  
University of Glasgow  
Glasgow G12 8QQ, UK  
S. W. Im  
Department of Materials Science and Engineering  
Seoul National University  
Seoul 08826, Republic of Korea  
M. Urbanova  
Department of Physics and Measurements  
University of Chemistry and Technology  
Prague 16628, Czech Republic

 The ORCID identification number(s) for the author(s) of this article can be found under <https://doi.org/10.1002/adom.202202991>.

© 2023 The Authors. Advanced Optical Materials published by Wiley-VCH GmbH. This is an open access article under the terms of the Creative Commons Attribution License, which permits use, distribution and reproduction in any medium, provided the original work is properly cited.

DOI: 10.1002/adom.202202991

important in CD for biological and chemical samples as it is challenging to achieve with nanophotonic platforms that are compatible with aqueous environments. The indirect strategy is a complete divergence from conventional chiroptical spectroscopic paradigms. It relies on detecting asymmetric changes in the response of left and right-handed (LH and RH) chiral plasmonic structures on the introduction of a chiral medium.<sup>[17]</sup> This differential response is due to chiral media inducing asymmetric changes in the intensities and chiral properties of the near fields of LH and RH substrates.<sup>[17]</sup> Since the indirect strategies do not rely on the nanophotonic structures being in resonance with an electronic transition of a molecule, gold plasmonic structures can be used, which widen the range of systems, both biological and chemical, which can be studied.<sup>[17]</sup> However, this approach does also have inherent weakness, primarily the complexity of the phenomena responsible for the observed effects. For instance, chiral detection is strongly dependent on the orientational order of the adsorbed target molecule,<sup>[5,18]</sup> and it is, surprisingly, dependent on the charged state of the molecule, indicating a capacitive contribution of the response which is not accounted for in previous EM numerical modeling.<sup>[19]</sup> An issue with some early studies employing the indirect strategy, was that local changes in near field properties were monitored by observing small changes in a far field optical response. Recently, it has been shown that directly probing changes in the local EM environment caused by chiral media with luminescence measurements, larger asymmetric responses can be achieved than with far field measurement methods.<sup>[20,21]</sup>

Here we demonstrate how surface enhanced Raman scattering (SERS) can be used to detect large asymmetric local changes in near field intensities of enantiomeric metafilms, containing chiral nanocavities, induced by the deposition of chiral helicoid nanoparticles. Thus, providing a novel

approach for the enantiomeric discrimination of plasmonic nanoparticles. The origin of the effect is the differential intensities of hot spots generated in gap regions formed where the helicoid and chiral metafilms are very close. Together, an achiral molecule, biphenyl-4,4'-dithiol (BPDT), acts both to facilitate binding between the helicoid nanoparticles and the metafilm, and as a Raman reporter of the near field intensities. This study provides a framework of using an alternative indirect approach, based on SERS, for exploiting nanostructures for chiral sensing.

## 2. Results and Discussion

In this study, we combine Au metafilms with chiral nanoparticles. The Au metafilms have multiple nanostructured arrays consisting of six armed “shuriken” shaped nanoindentation that are intrinsically either left-handed (LH) or right-handed (RH), **Figure 1A,B**; and **Figure S1** (Supporting Information). The substrates are based on nanopatterned polycarbonate templates, which have been described in detail elsewhere.<sup>[19,22,23]</sup> The metafilms are then formed by coating the templates with a 100 nm Au film and have previously been used in chirally sensitive biosensing to study structural changes in proteins, high-throughput nanoscale spatial functionalization strategies, and active plasmonics for controllable chiral optical response.<sup>[12,24]</sup> Recently, they have also been used to demonstrate how near field effects can enhance probing chiral media with higher sensitivity using functionalized quantum dots and measuring the plasmonically enhanced luminescence.<sup>[20]</sup> Reflectance spectra collected from shurikens in air, display multiple resonances over the visible and near infrared spectral region, **Figure 1F**, with sharper features between 700 and 770 nm region displaying Fano coupling between multiple modes, and a broader resonance between 500 and 650 nm.<sup>[19,20]</sup> This latter feature is

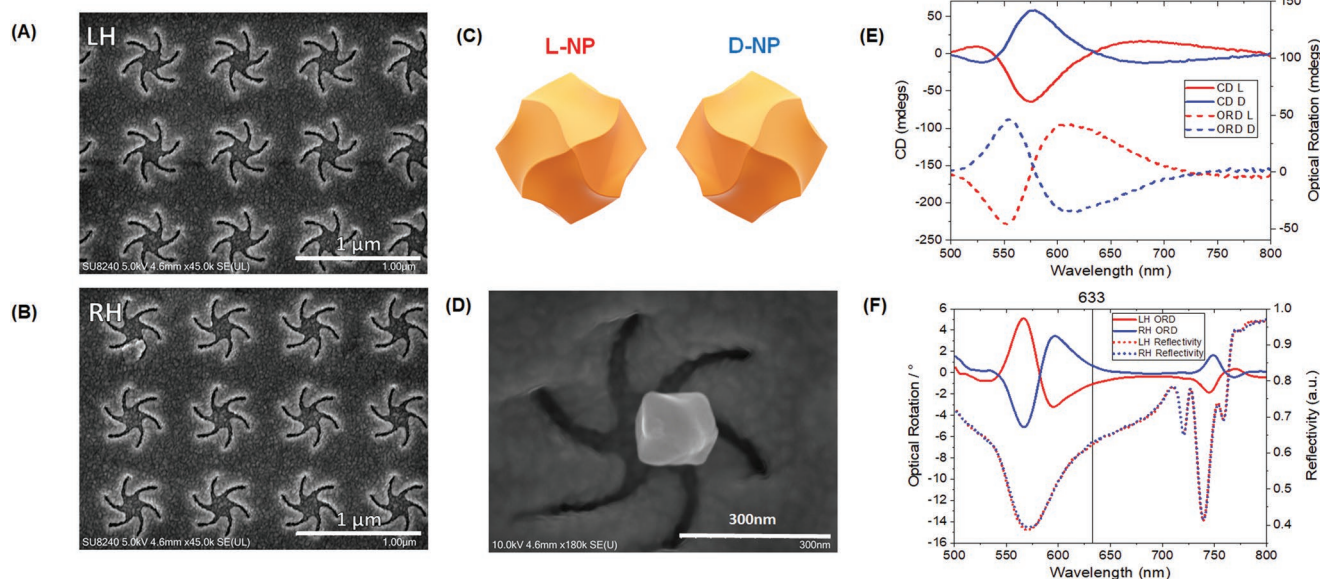


**Figure 1.** SEM images of shuriken A) LH and B) RH metafilms, C) idealized model images of L and D HNPs,<sup>[25,26]</sup> D) SEM image of a L-NP functionalized on a RH shuriken. E) CD and ORD (calculated using Kramers–Kronig transform) spectra for L- (red) and D- (blue) HNPs in aqueous solution, and F) ORD and reflectivity spectra for LH (red) and RH (blue) shuriken nanostructures (position of Raman excitation line is noted with a solid line).

associated with a resonance that has a bisignate line shape in optical rotation dispersion (ORD). As would be expected due to the chiral nature of the shurikens, LH and RH structures show equal and opposite ORD spectra.

Rhombic dodecahedral shaped, chiral nanoparticles, subsequently referred to as helicoidal nanoparticles (HNP), were made using an established synthesis strategy, Figure 1C,D.<sup>[25,26]</sup> Seed-mediated colloidal growth using an amino acid as the shape modifier helps control the handedness and chiral plasmonic resonance of the nanoparticles. In this work, chirality was conveyed on to the HNP by the presence of a chiral ligand, cysteine (L- or D-), with the absolute configuration of the particle being controlled by that of the ligand (Figure S2, Supporting Information). Consequently, particles generated with L-cysteine as an additive are termed L-HNPs and those generated using D-cysteine are termed D-HNPs. The CD responses (which are quoted in units of millidegrees) from these plasmonic nanoparticles are highest in the 500–650 nm spectral region, Figure 1E, overlapping with that shown by the shuriken metafilms. Functionalization of the HNPs to the metafilm is performed by first generating a self-assembled monolayer (SAM) using BPDT on the Au films. The adsorption of BPDT caused red shifts of  $\approx 2.2$  nm on both LH and RH shuriken metafilms, indicative of no significant difference in coverage between the enantiomorphs. The nanoparticles are then functionalized using the second thiol group of the now bound BPDT and any weakly bound HNPs are subsequently rinsed away. The combination of HNP and shuriken can be regarded as a diastereomer. As a convention, a two-lettered labeling system is used to describe the different diastereomeric combinations of shuriken and HNP, “LL,” “LR,” “RL,” and “RR,” where the first letter describes the handedness of the shuriken nanostructure

and the second letter the handedness of the nanoparticle. For simplicity D-HNP is considered a right-handed particle and referred to by “R.” The HNP deposition process produced structurally heterogeneous layers with particles being immobilized at random positions both within the shuriken indentation and in the regions between structures, Figure 2A; and Figure S4 (Supporting Information) for higher magnification micrographs). The deposition of HNPs induced broadening in the reflectivity (Figure S3, Supporting Information), as evidenced by a loss of resolution in the structure of the resonance at 700–770 nm. Given the HNP does not have a resonance in this region, the observed broadening is likely associated with coupling between the HNPs and metafilms,<sup>[27]</sup> and redshift the bisignate ORDs, Figure 2B, by  $\approx 1.6$  nm for all diastereomeric combinations, indicative of both an absence of asymmetry in the far field linear response and similar coverages of HNP for the four combinations. SERS response of the achiral BPDT was measured and to mitigate any possible variations in HNP coverage on metafilms, the Raman measurements were performed on multiple sites of each of the L- or D-HNPs coated substrates. Each substrate has nine pairs of LH and RH shuriken arrays (Figure S5, Supporting Information) and Raman measurements were performed at a single position on all pairs to collect nine spectra of each diastereomeric combinations (36 in total), Figure 3A–D. The solid lines show the means of the Raman measurements, and the standard errors are shown by the shaded bands surrounding each solid line. Similar spectra, in terms of positions of bands and relative intensities, were obtained from all substrates, and they are solely dominated by bands associated with BPDT. The BPDT SERS spectra in this work are very similar to those obtained previously from BPDT immobilized on either Au nanoparticles or commercial

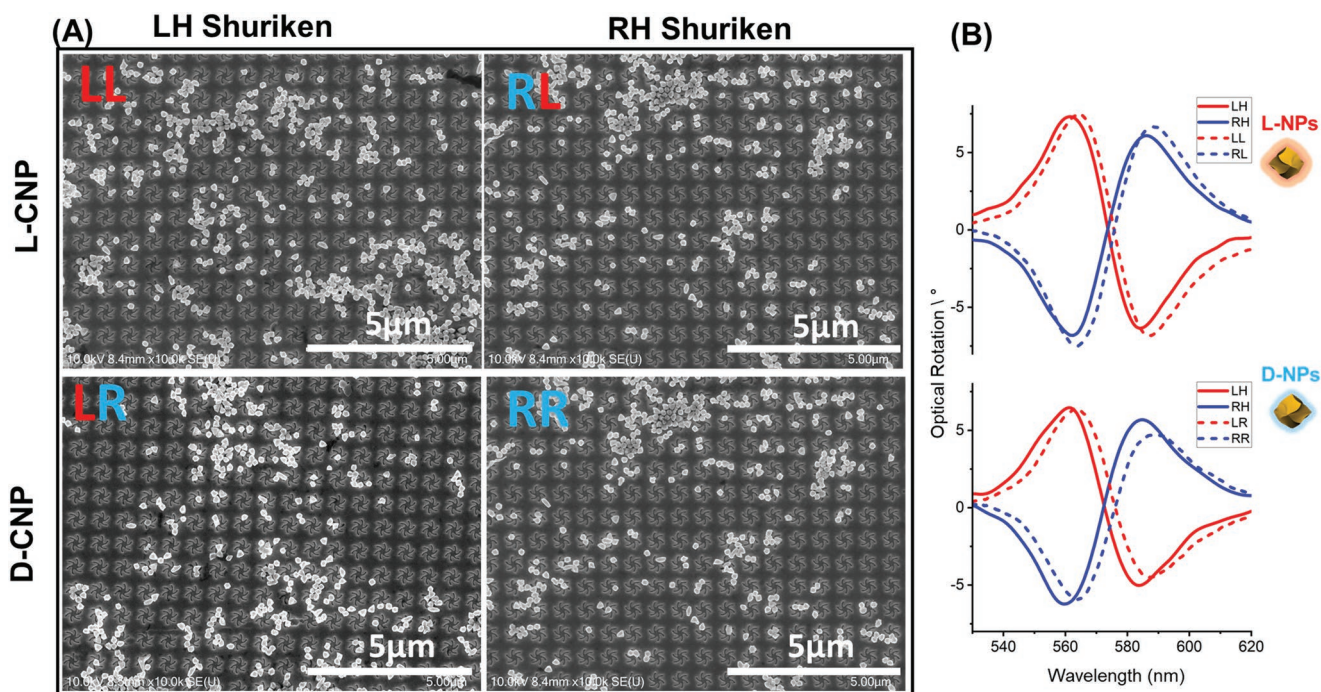


**Figure 2.** A) SEM images of LH and RH nanostructures functionalized with BPDT and HNPs. B) ORD spectra from pristine (solid lines) and HNP functionalized (dotted lines) LH (red) and RH (blue) shurikens samples.

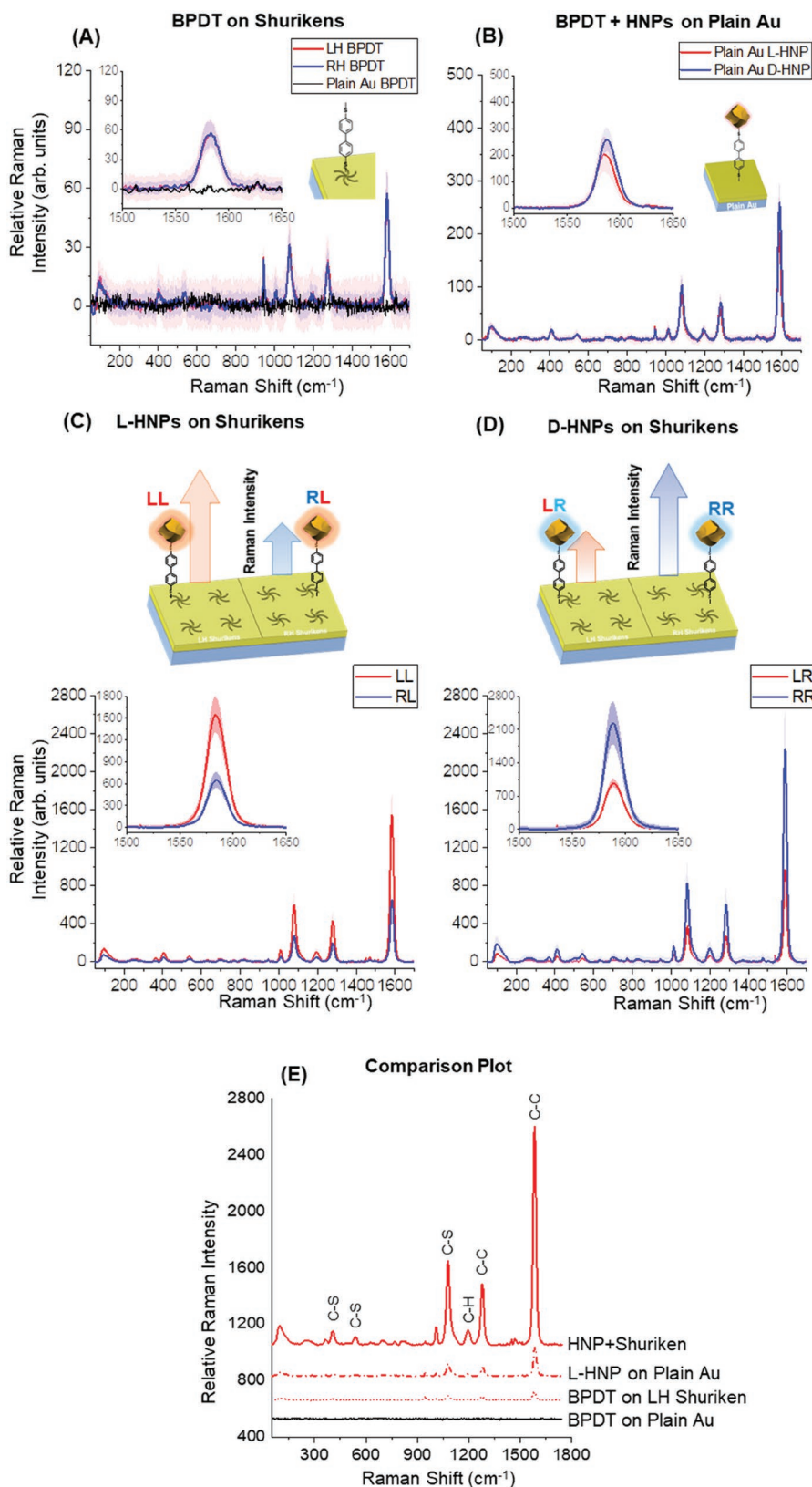


**Figure 3.** BPDT SERS spectra for: A) LH and RH shuriken only metafilms, B) L (L)- and D (R)-HNP deposited on unstructured Au films. C) L-HNPs and D) D-HNPs on the LH and RH shurikens, where solid lines show the mean values of the 9 data sets and the shaded bands represent the standard error. Inset graphs zoom on to the largest peaks from the spectra. E) Comparison of SERS intensities between HNP functionalized on shurikens, HNPs on plain Au, BPDT on the shurikens and BPDT on plain Au,

SERS (Klarite) substrates.<sup>[28]</sup> They display characteristic strong Raman peaks at  $\approx 1589$ , 1285, 1200, and 1084  $\text{cm}^{-1}$ , vibrational assignments are given in Table S1 and Figure S6 (Supporting Information).

No Raman spectra were detectable from BPDT layers on unstructured Au films in the absence of HNPs, Figure 3A. As references, Raman spectra were collected from BPDT functionalized LH and RH shurikens in the absence of HNPs, Figure 3A, and from L- and D-HNPs immobilized on BPDT layers on unstructured Au films, Figure 3B. L- and D-HNPs on unstructured Au surfaces give Raman spectra which, within experimental error, have near identical intensities. The Raman spectra obtained from BPDT from the two shuriken diastereomers symmetry pairs, that is shurikens and HNPs, Figure 3C,D, have intensities which are within the standard errors of each other. Differences between the two L- and D-HNP derived samples and the relatively large standard error can be attributed to the level of heterogeneity of the deposited HNP layers. There is no significant variation in the intensity of the Raman bands after 10 measurements are made consecutively in the same spot (see Figure S7, Supporting Information)

The central result of this study is the observation of the dependencies of the overall intensities of the Raman spectra on the symmetry properties of the diastereomer combinations of HNP and shuriken. In Figure 3C, a comparison of spectra from L-HNP on both shuriken enantiomorphs is shown, while the equivalent comparison for the D-HNP (R) is shown in Figure 3D. The SERS spectra clearly show that the matched combinations, LL and RR, of nanostructures and HNPs result in higher Raman signal intensities compared to their mismatched counterparts, LR and RL. The average ratios of the Raman intensities of all the bands for LR/RR and RL/LL combinations are given in Table S2 in the Supporting Information. The average ratios for the LR/RR and RL/LL combinations are  $0.50 \pm 0.02$  and  $0.47 \pm 0.02$ , respectively.

A final point about the Raman data is the dependency of the magnitudes of the responses on the type of substrates, Figure 3E. The following trend in the intensities of the BPDT

Raman signal is observed; HNP + Shurikens (Average) > HNP + Flat substrate > Shuriken only. Specifically, average signal from the HNP + Shuriken is  $\approx 7.5$  times greater than that from HNP on unstructured Au, which is in turn  $\approx 4.5$  times greater than the response from BPDT on shurikens. The observation that shuriken only structure gives the weakest Raman response can be readily reconciled when one considers that these structures produce weaker hot spots than the other two cases. This is because the hotspots associated with the shuriken structures (without HNPs) are predominately in the arms. The width of the arms is much larger than the gap regions formed between the HNP and either the Au unstructured or shuriken surface. To confirm that the intensity asymmetries in spectra derived from single position measurements, Figure 3C,D, are not due to sample-to-sample heterogeneity in the coverages of HNP, we have collected Raman spectra from 10 positions on the metafilms, which effectively cover the whole area of the array, Figure 4A. The averages of these 10 spectra show both the same asymmetries and have signal intensities within experimental error to those observed in the single point measurements, Figure 4B,C.

We propose that the dependency of the Raman reporter signal on the symmetry properties of the diastereomeric combinations of HNP and shuriken arises from the different EM environments that they possess. It is well established that light-matter coupling is strongly enhanced in resonant cavities and antennae.<sup>[29,30]</sup> Enhancement of spontaneous emission for instance can be engineered using Forster resonance energy transfer or the Purcell effect by placing the emitter in a resonant cavity generating large local density of optical states.<sup>[31,32]</sup> In the case of enhanced Raman scattering from plasmonic cavities/antennae, it can be shown that the total observable enhancement is a cumulative result of field enhancement of the incoming radiation and the enhanced radiative decay rate at the Stokes frequency.<sup>[33,34]</sup> The relative size of a SERS response is generally discussed in terms of an enhancement factor (EF), which is the relative size of a signal compared to that obtained from conventional Raman measurement. If the frequency of

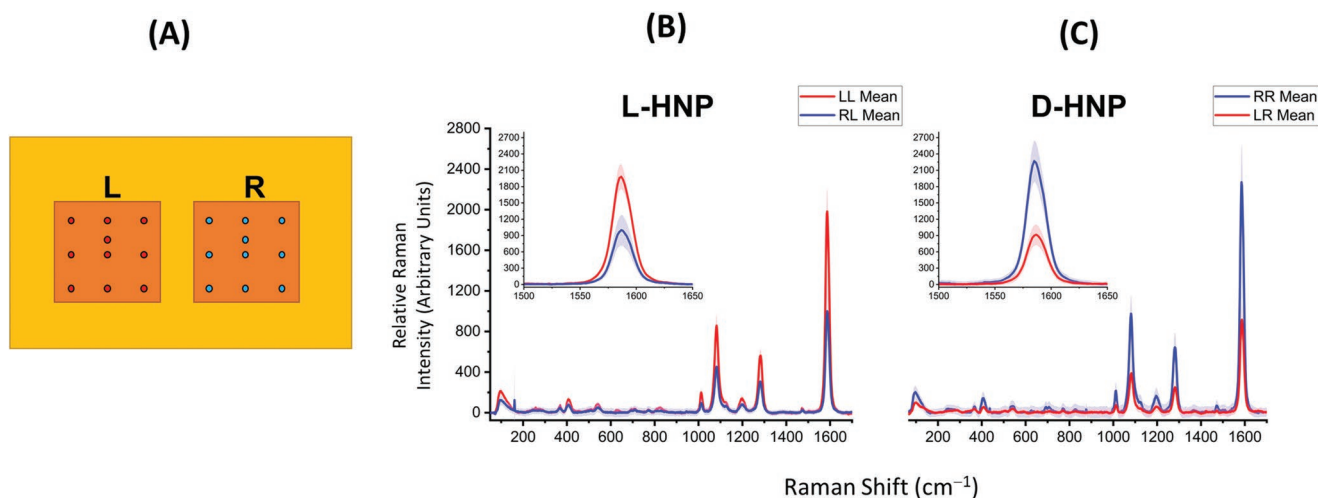


**Figure 4.** A) The 10 positions where Raman spectra were collected on left (L) and right (R) handed metafilms. B) L-HNPs and C) D-HNPs on the L and R shurikens, where solid lines show the mean values of the 10 data sets and the shaded bands represent the standard error. Inset graphs zoom on to the largest peaks from the spectra.

the Raman scattered light is close to that of the incident light, then<sup>[35]</sup>

$$EF \approx \left| \frac{E_{loc}}{E_i} \right|^4 \quad (1)$$

where  $E_{loc}$  is the electric local field amplitude at the Raman active site (or hot spot) and  $E_i$  is the amplitude of the incident excitation. Hence, Equation (1) relates the EF to intensities of hotspot regions in the EM environment. Consequently, our hypothesis is that

$$\left| \frac{E_{loc}}{E_i} \right|_{LL,RR} > \left| \frac{E_{loc}}{E_i} \right|_{LR,RL} \quad (2)$$

an argument that can be validated through numerical EM simulations. Given the structural complexity of the deposited layers, simulations of the different symmetry combinations were performed using a single HNP placed in close vicinity to a shuriken nanostructure, **Figure 5A**, as a simplified representation of our experimental samples. When simulating the HNPs on the shuriken nanostructure with a 633 nm excitation, the most intense hotspot, **Figure 5B**, were found in the narrow gap regions between the shuriken film and the HNP. As would be expected the average  $\left| \frac{E_{loc}}{E_i} \right|^4$  values derived for symmetry related diastereomeric pairs are very similar, **Figure 5C**. We assign the slight difference in value between mirror symmetry related diastereomers to the computational constraints placed on mesh element size. The simulations clearly show that the most intense hotspots, thus the strongest Raman responses, are produced by diastereomers formed from matched pairs. From the information provided by the simulations we can calculate the ratio of the signal from mis-matched and matched pairs

(LR/RR and RL/LL). Assuming the Raman response is dominated by contribution from these hotspots and the intensity of the signal is dependent on  $\left| \frac{E_{loc}}{E_i} \right|^4$  values for LR/RR and RL/LL are 0.67 and 0.69. These values are derived by taking an average value in an area defined by the red box in **Figure 5C**, which contains the hotspots, but also significant areas within the Au structures where there is no significant field. Consequently, one would expect the actual ratios in the hotspot region to be lower than have been calculated. Thus, with this caveat, the ratios obtained from the simulations are in reasonable agreement with the experimental observed values of 0.43 and 0.46.

To assess the influence of HNP position on the level of asymmetries of the near field intensities, simulations with HNP which have been rotated by  $\approx 45^\circ$  relative to the previous structural model have been performed (**Figure S9**, Supporting Information). In contrast to the previous model, the HNP in these simulations do not have the same distances to the surface of the shuriken in matched and mismatched pairs. For matched combinations the HNP is closer to the shuriken walls compared to the mismatched cases. These simulations also show a higher near field intensities for matched symmetry combinations. Given the closer separation one would expect that this model would favor higher field intensities for the matched relative to mismatched combinations (i.e., one would expect the LR/RR and RL/LL ratios to be smaller than in the previous model). However, counter-intuitively this is not the case, with LR/RR and RL/LL ratios being 0.76 and 0.78, respectively.

Finally, we have performed simulations in which the HNPs are in the middle of the arms of the shuriken rather than in the central cavity, **Figure 6**. The HNP used in the simulation is identical to that used for the data in **Figure 4**. These simulations also show matched symmetry combinations produce more intense fields with LR/RR and RL/LL ratios of 0.75

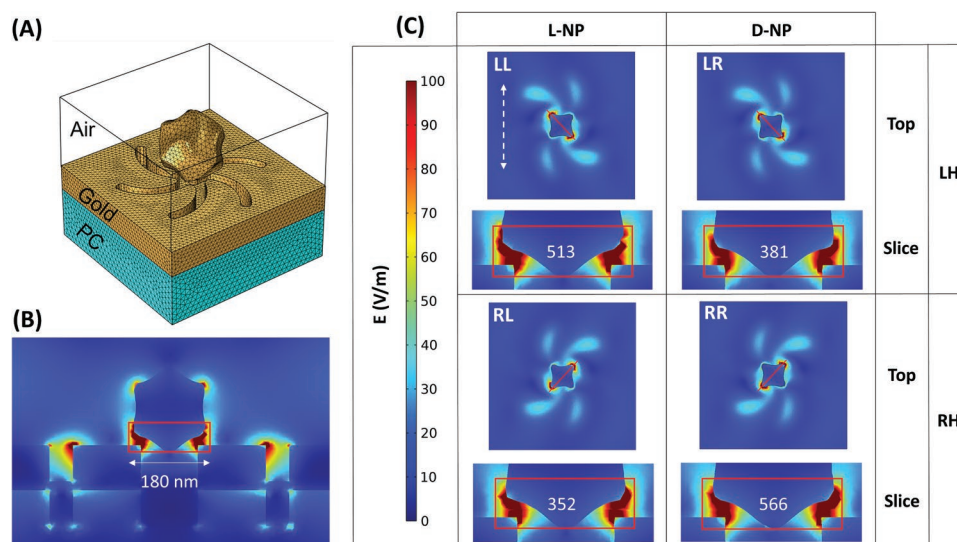


**Figure 5.** A) The idealized structural model used in the simulations with HNP on nanostructure on a polycarbonate (PC) substrate, with 720 nm periodicity and a HNP end to end length of  $\approx 160$  nm. B) A side view of a slice of the simulated  $|E|$  for the RR diastereomeric combination, the red box highlights region with the most intense hotspots. C) Simulated maps of  $|E|$  for the four diastereomeric combinations, the top views are shown above the sliced views which is highlighted by the red box ( $55 \times 180$  nm) in (B). The numbers shown lower panels are  $\left| \frac{E_{loc}}{E_i} \right|^4$  values obtained by averaging fields over the area of the red box. The polarization of the incident light is highlighted with the dashed white arrow in the top left panel of (C).

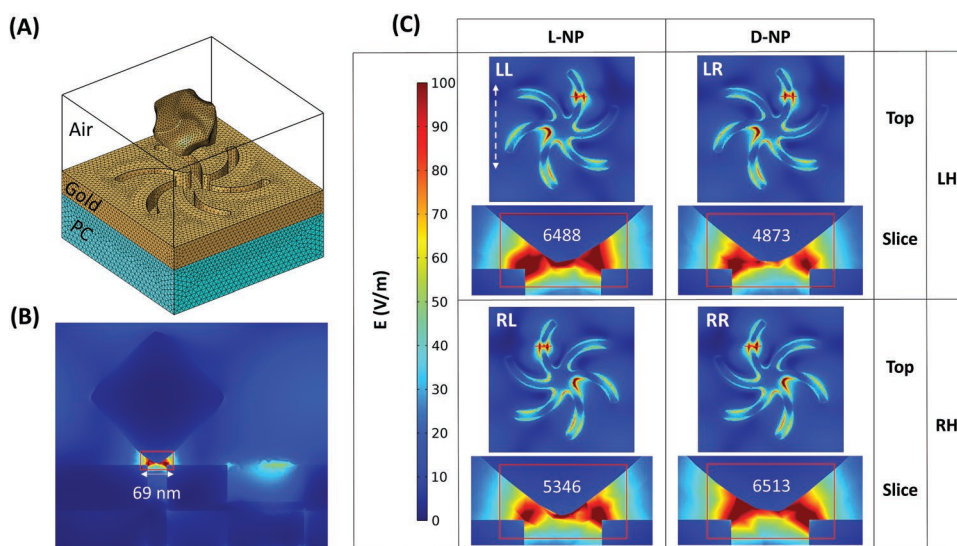


**Figure 6.** A) The idealized structural model used in the simulations with HNP on nanostructure on a polycarbonate (PC) substrate, with 720 nm periodicity and a HNP end to end length of  $\approx 160$  nm. B) A side view of a slice of the simulated  $|E|$  for the LL diastereomeric combination, the red box highlights region with the most intense hotspots. C) Simulated maps of  $|E|$  for the four diastereomeric combinations, the top views are shown above the sliced views which is highlighted by the red box ( $35 \times 69$  nm) in (B). The numbers shown lower panels are  $\left| \frac{E_{\text{loc}}}{E_i} \right|^4$  values obtained by averaging fields over the area of the red box. The polarization of the incident light is highlighted with the dashed white arrow in the top left panel of (C).

and 0.82, respectively. This geometry results  $\left| \frac{E_{\text{loc}}}{E_i} \right|^4$  values which are approximately one order of magnitude greater than the equivalent produced by the two previous models with the HNP located in the shuriken cavity.

So, although based on highly idealized models the numerical simulations support our hypothesis that diastereomeric pairs, which are not related by mirror symmetry, have different EM near field environments which can be detected using the SERS response from a reporter molecule.

### 3. Conclusion

Before the advent of routine chiroptical characterization, chemists determined the unknown absolute configurations of chiral molecules by combining them with other chiral species of known handedness to produce diastereomers. While the enantiomers of chiral compounds had identical physical and electronic properties, the diastereomers produced from them did not. Thus, allowing physical and spectroscopic methods to discriminate between them, and the absolute configurations to be determined. The work we present is a 21st century EM analogue of this well-established chemical strategy. We have achieved enantiospecific recognition by discriminating between the different near field environments possessed by diastereomers which are not related by mirror symmetry. By using SERS and an appropriate reporter molecule, we have achieved chiral recognition by detecting “cooler” and “hotter” hotspots. The near field sensitivity of SERS makes it a more sensitive probe to local changes in EM environment than reflectance measured in the far field which monitors a much larger volume of the near field. It should be stressed that the SERS

measurements reported here are not intrinsically optically active (i.e., chirally sensitive), and thus contrast with previous work which used metamaterials to amplify the sensitivity of SEROA measurements.<sup>[36]</sup> The advantage of the approach of leveraging “meta-diastereomers” used in this study is that the asymmetric responses are vastly larger by 2 orders of magnitude than are observed in SEROA. Although our study involves a chiral plasmonic HNP the SERS approach we outline would also be valid for detecting local changes in near fields of chiral metafilms induced by chiral molecules. Consequently, the SERS-based strategy demonstrated in this work would enable rapid recognition of chiral nanoparticles and compounds using very small sample quantities with applications in drug development and biostructural analysis.

### 4. Experimental Section

**Fabrication of Chiral Metafilms:** The templated substrates were prepared by injection molding. Clean silicon substrates were coated with  $\approx 80$  nm of PMMA (Elvacite 2041, Lucite International) and electron beam writing was performed on a Vistec VB6 UHR EWF lithography tool operating at 100 kV. The substrates were then developed using a mixture of methyl isobutyl ketone and isopropyl alcohol to complete the Si master. 300  $\mu\text{m}$  thick nickel shim was formed through electroplating on the Si master. The shim was mounted in a custom-made tool used with an Engel Victory Tech 28 tons injection molding machine in a fully automatic production mode to manufacture polymer slides using polycarbonate (Makrolon DP2015) as feedstock. The injection molded substrates have chiral nanostructures imparted in the plastic surface and were subsequently covered by a continuous 100 nm Au film to complete the metafilm sample production.

**Synthesis of Chiral Nanoparticles:** Hexadecyltrimethylammonium bromide (CTAB, 99%), L-ascorbic acid (AA, 99%), D-cysteine (99%) L-cysteine (98.5%), tetrachloroauric(III) trihydrate ( $\text{HAuCl}_4 \cdot 3\text{H}_2\text{O}$ ,

99.9%), biphenyl-4,4'-dithiol (95%), and ultrapure water (LiChrosolv) were purchased from Sigma-Aldrich and used without further purification.

Cubic seeds were synthesized as reported previously.<sup>[37,38]</sup> Further synthesis was performed according to the published procedure with some modifications.<sup>[26]</sup> In the next step, a growth solution was prepared: 0.8 mL of 100 mM CTAB and 0.2 mL of 10 mM gold chloride trihydrate were added into 3.95 mL of deionized water. Then 0.475 mL of 100 mM ascorbic acid solution was added to the growth solution to reduce Au<sup>3+</sup>. Further, to prepare chiral nanoparticles, 0.05 mL of cubic seeds were added to the growth solution, and after a 20 min incubation, 0.005 mL of cysteine were added. The growth solution was left for 2 h at 30 °C, during this time, the solution changed color from pink to blue. The solution was centrifuged twice (3000 rpm, 180 s) and was dispersed in a 1 mM CTAB solution for further characterization.

**Sample Preparation:** Au-coated shurikens were first rinsed with methanol and plasma cleaned for 5 min at 100 W power. Shurikens were then immersed in a 3 mM methanol solution of biphenyl-4,4'-dithiol (95%) (Sigma-Aldrich) for 24 h to form a self-assembled monolayer (SAM). After rinsing and drying the shurikens with methanol solutions of nominal concentrations of 30 mg mL<sup>-1</sup> of either L- or D-chiral nanoparticles in DI water was added. The samples were left on a shaker for 24 h, then washed and dried with DI water.

**Surface Characterization Techniques:** SEM images for shurikens were acquired with a SU8240 (Hitachi) using 10 kV acceleration.

**Measurements of Optical Spectra:** A custom built polarimeter, equipped with a tungsten halogen light source (Thorlabs), polarizers (Thorlabs), and a 10x objective (Olympus) was used to collect ORD measurements and reflectivity spectra. The samples are positioned and aligned with the aid of a camera (Thorlabs), and the spectrum was measured using a compact spectrometer (Ocean optics USB4000). Reflectivity measurements used plain Au as a background. ORD spectra were obtained using the Stokes' method. Linearly polarized light was positioned incident on the substrate, and the intensities of the reflected light at four polarization angles (0°, ±45°, and 90°) relative to the incident light were measured to calculate the ORD. The final spectrum is the mean of 8 measurements for a single nanostructure array.

**Raman Measurement:** Raman spectra were recorded using a NT-MDT NTEGRA Raman microscope with a 633 nm laser excitation (35 mW power) with 10 s accumulation time. Excitation and collection of Raman scattered light was done using a 20x objective with an estimated spot size of 100 μm. From each sample, 9 LH and RH shuriken array pairs were measured (18 measurements total measurements each sample). For analysis, the mean and standard error of the SERS intensity values were calculated.

**Numerical Electromagnetic Modeling:** A commercial finite element package (COMSOL V6.0 Multiphysics software, Wave Optics module) was used to simulate the EM fields produced across the sample. Periodic boundary conditions were applied to shuriken boundaries to replicate metamaterial conditions. Perfectly matched layer (PML) conditions were applied to both input and output ports to minimize internal reflections.

The shuriken metafilms along with a 240 nm diameter chiral L- or D-nanoparticle positioned 250 nm above the shuriken center (Figure S8, Supporting Information) were simulated. Due to computational constraints, the NP could not be positioned 1 nm away from the gold surface (as expected experimentally). Maps showing the distribution of the electric field have been plotted for all the combinations of shuriken and NP handedness. These maps depict where the hot spots (HS) are located between the NP and the metafilm surface. A vertical slice across the HS was obtained, and the average value of the amplitude of the electric field was computed and compared for all the combinations (Figure 4).

## Supporting Information

Supporting Information is available from the Wiley Online Library or from the author.

## Acknowledgements

M.K. and A.S. would like to acknowledge ScotCHEM and the Scottish Government for funding received under the SFC Saltire Emerging Researcher ScotCHEM European Exchanges Scheme. A.K. would like to acknowledge support by the UKRI, EPSRC (Nos. EP/S001514/1 and EP/S029168/1) and the James Watt Nanofabrication Centre. N.G. and M.K. acknowledge support from EPSRC (Nos. EP/S012745/1 and EP/S029168/1). M.K. also acknowledges the Leverhulme Trust (No. RF-2019-023). O.L. would like to acknowledge support by the GACR under the project 20-19353S. The authors would also like to thank Prof. Laurence D. Barron for his insightful discussions that have helped advance the work.

## Conflict of Interest

The authors declare no conflict of interest.

## Data Availability Statement

The data that support the findings of this study are available in the Supporting Information of this article.

## Keywords

chirality, enantiomer detection, plasmonics, surface enhanced Raman scattering

Received: December 13, 2022

Revised: January 20, 2023

Published online: March 14, 2023

- [1] N. Berova, L. Di Bari, G. Pescitelli, *Chem. Soc. Rev.* **2007**, *36*, 914.
- [2] T. B. Freedman, X. L. Cao, R. K. Dukor, L. A. Nafie, *Chirality* **2003**, *15*, 743.
- [3] J. García-Guirado, M. Svedendahl, J. Puigdollers, R. Quidant, *Nano Lett.* **2018**, *18*, 6279.
- [4] J. Garcia-Guirado, M. Svedendahl, J. Puigdollers, R. Quidant, *Nano Lett.* **2019**, *20*, 585.
- [5] C. Kelly, R. Tullius, A. J. Laphorn, N. Gadegaard, G. Cooke, L. D. Barron, A. S. Karimullah, V. M. Rotello, M. Kadodwala, *J. Am. Chem. Soc.* **2018**, *140*, 8509.
- [6] Z. Liu, J. Ai, P. Kumar, E. You, X. Zhou, X. Liu, Z. Tian, P. Bouř, Y. Duan, L. Han, A. N. Kotov, S. Ding, S. Che, *Angew. Chem.* **2020**, *132*, 15338.
- [7] W. Ma, H. Kuang, L. Xu, L. Ding, C. Xu, L. Wang, N. A. Kotov, *Nat. Commun.* **2013**, *4*, 2689.
- [8] M. Silverman, *Opt. Commun.* **1989**, *74*, 134.
- [9] D. R. Smith, N. Kroll, *Phys. Rev. Lett.* **2000**, *85*, 2933.
- [10] M. L. Solomon, A. A. Saleh, L. V. Poulikakos, J. M. Abendroth, L. F. Tadesse, J. A. Dionne, *Acc. Chem. Res.* **2020**, *53*, 588.
- [11] X. Sun, H. Kong, Q. Zhou, S. Tsunega, X. Liu, H. Yang, R.-H. Jin, *Anal. Chem.* **2020**, *92*, 8015.
- [12] R. Tullius, A. S. Karimullah, M. Rodier, B. Fitzpatrick, N. Gadegaard, L. D. Barron, V. M. Rotello, G. Cooke, A. Laphorn, M. Kadodwala, *J. Am. Chem. Soc.* **2015**, *137*, 8380.
- [13] R. Tullius, G. W. Platt, L. Khosravi Khorashad, N. Gadegaard, A. J. Laphorn, V. M. Rotello, G. Cooke, L. D. Barron, A. O. Govorov, A. S. Karimullah, M. Kadodwala, *ACS Nano* **2017**, *11*, 12049.
- [14] T.-H. Xiao, Z. Cheng, Z. Luo, A. Isozaki, K. Hiramatsu, T. Itoh, M. Nomura, S. Iwamoto, K. Goda, *Nat. Commun.* **2021**, *12*, 3062.



- [15] Y. Zhao, A. N. Askarpour, L. Sun, J. Shi, X. Li, A. Alù, *Nat. Commun.* **2017**, *8*, 14180.
- [16] M. L. Solomon, J. M. Abendroth, L. V. Poulikakos, J. Hu, J. A. Dionne, *J. Am. Chem. Soc.* **2020**, *142*, 18304.
- [17] N. N. Jiang, X. L. Zhuo, J. F. Wang, *Chem. Rev.* **2018**, *118*, 3054.
- [18] T. Kakkar, C. Keijzer, M. Rodier, T. Bukharova, M. Taliany, A. J. Love, J. J. Milner, A. S. Karimullah, L. D. Barron, N. Gadegaard, A. J. Laphorn, M. Kadodwala, *Light: Sci. Appl.* **2020**, *9*, 195.
- [19] M. Rodier, C. Keijzer, J. Milner, A. S. Karimullah, A. W. Roszak, L. D. Barron, N. Gadegaard, A. J. Laphorn, M. Kadodwala, *Nanoscale Horiz.* **2020**, *5*, 336.
- [20] M. Hajji, M. Cariello, C. Gilroy, M. Kartau, C. D. Syme, A. Karimullah, N. Gadegaard, A. Malfait, P. Woisel, G. Cooke, W. J. Peveler, M. Kadodwala, *ACS Nano* **2021**, *15*, 19905.
- [21] V. Tabouillot, R. Kumar, P. L. Lalaguna, M. Hajji, R. Clarke, A. S. Karimullah, A. R. Thomson, A. Sutherland, N. Gadegaard, S. Hashiyada, M. Kadodwala, *ACS Photonics* **2022**, *9*, 3617.
- [22] A. S. Karimullah, C. Jack, R. Tullius, V. M. Rotello, G. Cooke, N. Gadegaard, L. D. Barron, M. Kadodwala, *Adv. Mater.* **2015**, *27*, 5610.
- [23] C. Kelly, L. Khosravi Khorashad, N. Gadegaard, L. D. Barron, A. O. Govorov, A. S. Karimullah, M. Kadodwala, *ACS Photonics* **2018**, *5*, 535.
- [24] C. Jack, A. S. Karimullah, R. Tullius, L. K. Khorashad, M. Rodier, B. Fitzpatrick, L. D. Barron, N. Gadegaard, A. J. Laphorn, V. M. Rotello, G. Cooke, A. O. Govorov, M. Kadodwala, *Nat. Commun.* **2016**, *7*, 10946.
- [25] H.-E. Lee, R. M. Kim, H.-Y. Ahn, Y. Y. Lee, G. H. Byun, S. W. Im, J. Mun, J. Rho, K. T. Nam, *Nat. Commun.* **2020**, *11*, 263
- [26] H.-E. Lee, H.-Y. Ahn, J. Mun, Y. Y. Lee, M. Kim, N. H. Cho, K. Chang, W. S. Kim, J. Rho, K. T. Nam, *Nature* **2018**, *556*, 360.
- [27] C. Dahmen, B. Schmidt, G. von Plessen, *Nano Lett.* **2007**, *7*, 318.
- [28] Y. R. Lee, M. S. Kim, C. H. Kwon, *Bull. Korean Chem. Soc.* **2013**, *34*, 470.
- [29] Y. Yu, S. Mallick, M. Wang, K. Börjesson, *Nat. Commun.* **2021**, *12*, 3255
- [30] X. Gan, K. F. Mak, Y. Gao, Y. You, F. Hatami, J. Hone, T. F. Heinz, D. Englund, *Nano Lett.* **2012**, *12*, 5626.
- [31] T. V. Shahbazy, *Phys. Rev. Lett.* **2016**, *117*, 207401.
- [32] M. Li, S. K. Cushing, N. Wu, *Analyst* **2015**, *140*, 386.
- [33] S. A. Maier, *Opt. Express* **2006**, *14*, 1957.
- [34] J. Langer, D. J. de Aberasturi, J. Aizpurua, R. A. Alvarez-Puebla, B. Auguie, J. J. Baumberg, G. C. Bazan, S. E. J. Bell, A. Boisen, A. G. Brolo, J. Choo, D. Cialla-May, V. Deckert, L. Fabris, K. Faulds, F. J. G. de Abajo, R. Goodacre, D. Graham, A. J. Haes, C. L. Haynes, C. Huck, T. Itoh, M. Ka, J. Kneipp, N. A. Kotov, H. Kuang, E. C. Le Ru, H. K. Lee, J. F. Li, X. Y. Ling, et al., *ACS Nano* **2020**, *14*, 28.
- [35] S.-Y. Ding, E.-M. You, Z.-Q. Tian, M. Moskovits, *Chem. Soc. Rev.* **2017**, *46*, 4042.
- [36] T.-H. Xiao, Z. Cheng, Z. Luo, A. Isozaki, K. Hiramatsu, T. Itoh, M. Nomura, S. Iwamoto, K. Goda, *Nat. Commun.* **2021**, *12*, 3062.
- [37] H.-L. Wu, H.-R. Tsai, Y.-T. Hung, K.-U. Lao, C.-W. Liao, P.-J. Chung, J.-S. Huang, I.-C. Chen, M. H. Huang, *Inorg. Chem.* **2011**, *50*, 8106.
- [38] H.-Y. Ahn, H.-E. Lee, K. Jin, K. T. Nam, *J. Mater. Chem. C* **2013**, *1*, 6861.